International Journal of Pharmaceutics: X 2 (2020) 100064

Contents lists available at ScienceDirect

International Journal of Pharmaceutics: X

journal homepage: www.sciencedirect.com/journal/international-journal-of-pharmaceutics-x

Determination of the physical state of a drug in amorphous solid dispersions using artificial neural networks and ATR-FTIR spectroscopy

Afroditi Kapourani [a], Vasiliki Valkanioti [a], Konstantinos N. Kontogiannopoulos [a,b], Panagiotis Barmpalexis [a,*]

[a] Department of Pharmaceutical Technology, School of Pharmacy, Aristotle University of Thessaloniki, Thessaloniki 54124, Greece
[b] Ecoresources P.C., 15-17 Giannitson-Santaroza Str., Thessaloniki 54627, Greece

ARTICLE INFO

Keywords:
ATR-FTIR spectroscopy
Amorphous solid dispersions
Quantification method
Artificial neural networks
Partial least square regression
Principle component analysis

ABSTRACT

The objective of the present study was to evaluate the use of artificial neural networks (ANNs) in the development of a new chemometric model that will be able to simultaneously distinguish and quantify the percentage of the crystalline and the neat amorphous drug located within the drug-rich amorphous zones formed in an amorphous solid dispersion (ASD) system. Attenuated total reflectance Fourier-transform infrared (ATR-FTIR) spectroscopy was used, while Rivaroxaban (RIV, drug) and Soluplus® (SOL, matrix-carrier) were selected for the preparation of a suitable ASD model system. Adequate calibration and test sets were prepared by spiking different percentages of the crystalline and the amorphous drug in the ASDs (prepared by the melting - quench cooling approach), while a 2^4 full factorial experimental design was employed for the screening of ANN's structure and training parameters as well as spectra region selection and data preprocessing. Results showed increased prediction performance, measured based on the root mean squared error of prediction (RMSEp) for the test sample, for both the crystalline ($RMSEp_{(crystal)} = 0.86$) and the amorphous ($RMSEp_{(amorphous)} = 2.14$) drug. Comparison with traditional regression techniques, such as partial least square and principle component regressions, revealed the superiority of ANNs, indicating that in cases of high structural similarity between the investigated compounds (i.e., the crystalline and the amorphous forms of the same compound) the implementation of more powerful/sophisticated regression techniques, such as ANNs, is mandatory.

1. Introduction

The preparation of amorphous solid dispersions (ASDs) is a commonly used pharmaceutical formulation technique employed in order to increase active pharmaceutical ingredients' (APIs) oral bioavailability (Huang and Williams 3rd, 2018; Kawakami, 2017; Lin et al., 2018; Pandi et al., 2020; Ricarte et al., 2019). ASDs consist of an amorphous API stabilized by one (or more) excipient(s), of organic or inorganic nature, acting as matrix/carrier. This carrier is able to improve the physical stability and to maintain API's in vivo supersaturation when compared to the corresponding pure drug amorphous form (Kawakami, 2017; Newman et al., 2015; Ricarte et al., 2019). In this type of drug formulations, the solubility advantage is gained mostly due to drug's highly disordered amorphous state, and hence, its increased Gibbs free energy. However, the given advantage cannot be maintained indefinitely, since the amorphous API is thermodynamically unstable and tends to recrystallize (either during storage or during in vivo solubilization) into its more thermodynamically stable crystalline counterparts (Kawakami, 2017; Lin et al., 2018). In this context, although suitable ASD matrix/carriers have been carefully selected over the past years (Rahman et al., 2014), there are still several cases of ASD-based drug products that are being recalled due to insufficient physical stability (Guo et al., 2013; Siddiqui et al., 2014).

Looking to overcome these drawbacks, recent studies are paying more attention to the formation of a distinct, drug-rich, amorphous zone within the ASD systems (Dedroog et al., 2019; Meng et al., 2017; Wlodarski et al., 2018). Within this separate amorphous zone, API's recrystallization process begins, leading to system's physical instability. Therefore, the development of new standardized analytical measuring methods for the detection and quantification of the crystalline and amorphous portions of the API within the ASD system, is of crucial importance.

Several analytical techniques are currently being utilized for the determination and quantification of API's crystalline portion within any

* Corresponding author.
E-mail address: pbarmp@pharm.auth.gr (P. Barmpalexis).

https://doi.org/10.1016/j.ijpx.2020.100064
Received 17 September 2020; Received in revised form 27 November 2020; Accepted 28 November 2020
Available online 8 December 2020

ASD system. These include differential scanning calorimetry (DSC), near infrared (NIR), fourier-transform infrared (FTIR) and Raman spectroscopy, powder X-ray diffractometry (pXRD), solid-state nuclear magnetic resonance (ssNMR), scanning electron microscopy (SEM), terahertz spectroscopy etc. (Lust et al., 2015; Paudel and Geppi, 2014; Purohit and Taylor, 2015; Rahman et al., 2014; Sarpal et al., 2019; Sibik et al., 2015; Siddiqui et al., 2014; Song et al., 2016). Among them, and keeping in mind that an appropriate analytical method should be fast, non-destructive and able to simultaneously distinguish and quantify both crystalline and amorphous API forms, techniques based on vibrational spectroscopic seem to be more promising as compared to others (Zidan et al., 2012). However, although spectroscopic methods are attractive in terms of speed and simplicity their implementation might be problematic due to the difficulties arising from spectra peak overlapping (Bugay, 2001). This problem is significantly magnified in the case of ASDs since the two physical forms of the API (amorphous and crystalline) show, in most cases, almost similar spectra.

Nowadays, these peak overlapping problems are being handled via the utilization of data pretreatment techniques (including spectral subtraction, pattern matching processing etc.) along with several chemometric tools (such as partial least square, PLS; regression and principle component analysis, PCA, or regression PCR) (Rahman et al., 2010). Specifically, regarding ASDs, the, rather limited, attempts to develop a proper analytical method focus only on the quantification of the crystalline portion of the drug within the ASD system, via PCA and/or PLS regression analysis (Edinger et al., 2018; Lust et al., 2015; Netchacovitch et al., 2017; Rahman et al., 2014; Rahman et al., 2010; Rumondor and Taylor, 2010; Saerens et al., 2011; Siddiqui et al., 2014; Wabuyele et al., 2017; Zidan et al., 2012). To the best of our knowledge, until now there are no published attempts accounting for the simultaneous quantification of both the crystalline and the amorphous API within the ASD system, while, the utilization of modern and more efficient chemometric tools, based on machine learning algorithms (such as artificial neural networks, ANNs), has been neglected until now.

Therefore, the aim of the present study is to build for the first time a new chemometric model that will be able to distinguish and simultaneously quantify the percentage of the crystalline and the amorphous API located within the drug-rich amorphous zones of an ASD system. For this reason, attenuated total reflectance FTIR (ATR-FTIR) spectroscopy was evaluated as a suitable analytical method, while Rivaroxaban (RIV, an oxazolidinone derivative which binds directly and reversibly to Factor Xa (Perzborn et al., 2010; Samama, 2011)) and Soluplus® (SOL, polyvinylcaprolactam–polyvinyl acetate–polyethylene glycol graft copolymer) were utilized as suitable ASD model compounds (i.e., drug-matrix/carrier system). Finally, the present study attempts for the first time to evaluate the use of ANNs (i.e., biologically inspired computer algorithms working as universal function approximators) in similar drug quantification problems (Baskin et al., 2016; Xu et al., 2018; Yang et al., 2019) (Arabzadeh et al., 2019; Barmpalexis et al., 2018; Costa et al., 2019; Nagy et al., 2019; Toziou et al., 2018)), and to compare their efficacy with other, traditionally used, methods (i.e., PCR and PLS regression).

2. Material and methods

2.1. Materials

RIV form I crystals with $d_{90\%}$ of 52.7 μm (i.e., the portion of particles with diameters below 52.7 μm is 90%) measured via Malvern's Mastersizer 2000; Malvern, Malvern, UK) were kindly donated from Genepharm S.A. (Athens, Greece). The graft copolymer SOL (lot no. 84414368E0) containing 13% *w*/w PEG 6000, 57% w/w vinyl caprolactam and 30% w/w vinyl acetate, was obtained from BASF (Ludwigshafen, Germany). All other reagents used in the current study were of analytical or pharmaceutical grade and used as received.

Table 1
Composition of samples used for the development and validation of the new analytical method.

Code	RIV (% wt.)		ASD[a] (% wt.)
	Crystalline	Amorphous	
F1[b]	0.25	0.75	99.00
F2 [c]	0.50	0.50	99.00
F3 [c]	2.25	0.75	97.00
F4 [c]	1.50	1.50	97.00
F5 [c]	1.25	3.75	95.00
F6 [c]	2.50	2.50	95.00
F7[b]	5.25	1.75	93.00
F8[c]	3.50	3.50	93.00
F9[c]	2.00	6.00	92.00
F10[b]	4.00	4.00	92.00
F11[c]	7.50	2.50	90.00
F12[b]	5.00	5.00	90.00
F13[c]	3.75	11.25	85.00
F14[c]	7.50	7.50	85.00
F15[c]	15.00	5.00	80.00
F16 [c]	10.00	10.00	80.00
F17[c]	7.50	22.50	70.00
F18[c]	15.00	15.00	70.00
F19[b]	30.00	10.00	60.00
F20[c]	20.00	20.00	60.00
F21[b]	12.50	37.50	50.00
F22[c]	25.00	25.00	50.00
F23[c]	45.00	15.00	40.00
F24[b]	30.00	30.00	40.00
F25[c]	17.50	52.50	30.00
F26[c]	35.00	35.00	30.00
F27[c]	60.00	20.00	20.00
F28[c]	40.00	40.00	20.00
F29[b]	22.50	67.50	10.00
F30[c]	45.00	45.00	10.00

[a] ASD contained 20/80% wt. RIV/SOL
[b] Test subset
[c] Training subset

2.2. Preparation of amorphous RIV, ASDs and physical mixtures (PMs)

According to Rumondor et al., when building such quantification models, as the one attempted in the present study, it is important to prepare meaningful calibration and test samples which encompass all features of the investigated compounds (Rumondor and Taylor, 2010). Keeping in mind that ASDs cannot be described by a linear combination of the vibration spectra of the pure amorphous components (due to the presence of molecular interactions formed between the ASD components which alter significantly the corresponding spectra) the calibration and test samples must contain, instead of the pure amorphous copolymer (SOL), the actual ASD system mixed with both the crystalline and the amorphous forms of the API. Therefore, in the present study for the preparation of the respective calibration and test samples, ASDs of RIV and SOL were prepared via the melting (or co-melting) quench cooling approach. Briefly, appropriate amounts of RIV-SOL mixtures (corresponding to 20/80%wt API to copolymer) were sieved through 150 μm and mixed thoroughly with a mortar and pestle until a homogeneous blend was formed. The selection of the RIV to SOL weight ratio (i.e., 20/80% wt.) for the preparation of ASDs, was made in order to ensure that the API will be completely miscible within the matrix-carrier and that no amorphous phase separation phenomena will be observed within the time framework needed for the execution of the experiments and analysis. Subsequently, the prepared blends were heated in suitable aluminum pan at 245 °C for 3 min until a homogeneous miscible melt dispersion was obtained (verified visually via hot-stage polarized light microscopy, using a Linkam THMS600 heating stage (Linkam Scientific Instruments Ltd., Surrey, UK), mounted on Olympus BX41 polarized light microscope (Tokyo, Japan), and controlled through a Linkam TP94 temperature controller). The melt dispersion was then rapidly cooled in an ice bath and subsequently pulverized at room temperature with

Table 2
Experimental domain and RMSEp for the two-level full factorial design employed during ANN factor screening process.

Hidden units (X_1)	Iteration cycles (X_2)	Spectra region [1/cm] (X_3)	Transformation (X_4)	RMSEp	
				Crystalline	Amorphous
2	1000	800–1800	Untreated	1.22 ± 0.29	2.14 ± 0.57
2	5000	800–1800	Untreated	1.03 ± 0.01	2.81 ± 0.06
2	1000	2800–3500	Untreated	6.03 ± 0.45	3.32 ± 0.18
2	5000	2800–3500	Untreated	6.00 ± 0.02	3.74 ± 0.01
2	1000	800–1800	2nd derivative	0.98 ± 0.04	2.80 ± 0.03
2	5000	800–1800	2nd derivative	1.03 ± 0.01	2.74 ± 0.06
2	1000	2800–3500	2nd derivative	7.09 ± 0.71	5.38 ± 0.28
2	5000	2800–3500	2nd derivative	7.50 ± 0.10	5.44 ± 0.10
5	3000	800–1800	Untreated	6.74 ± 1.45	12.91 ± 1.52
5	3000	2800–3500	Untreated	5.63 ± 0.93	3.58 ± 0.27
5	3000	800–1800	2nd derivative	0.86 ± 0.15	2.69 ± 0.07
5	3000	2800–3500	2nd derivative	6.61 ± 0.87	6.94 ± 2.13
8	1000	800–1800	Untreated	3.00 ± 0.61	3.86 ± 0.07
8	5000	800–1800	Untreated	6.38 ± 0.14	11.41 ± 0.09
8	1000	2800–3500	Untreated	6.64 ± 0.73	3.93 ± 0.26
8	5000	2800–3500	Untreated	6.28 ± 1.72	4.05 ± 0.48
8	1000	800–1800	2nd derivative	1.01 ± 0.06	2.80 ± 0.02
8	5000	800–1800	2nd derivative	2.19 ± 0.72	4.28 ± 1.00
8	1000	2800–3500	2nd derivative	7.00 ± 0.68	4.51 ± 0.99
8	5000	2800–3500	2nd derivative	6.11 ± 0.72	6.83 ± 0.50

mortar and pestle, before sieving through 300 μm sieve. A similar procedure (without the addition of SOL) was used for the preparation of the amorphous RIV. Thermogravimetric analysis (TGA, Shimadzu TGA-50 thermogravimetric analyzer, Tokyo, Japan) confirmed the thermal stability of the API during both the amorphization and ASD preparation processes. Appropriate amounts (based on Table 1) of crystalline and amorphous RIV were then gently mixed with the prepared ASD system using a mortar and a pestle, and the resulting fine powder was passed through a 150 μm sieve. It is important to note that samples F23-F30 were prepared only for the extension of the model, since they are highly prone to physical instability. The collected samples were placed in hermetically sealed amber glass vials and stored in desiccators at room temperature (25 °C) in order to prevent moisture absorption prior to analysis.

2.3. Verification of RIV amorphization and crystallinity

The verification of the API's physical state for: i) the pure amorphous RIV, ii) the prepared ASDs, and iii) the pure amorphous and the crystalline API after mixing with the ASD system, was made via powder X-ray diffractometry (pXRD) using a Rigaku Mini Flex II diffractometer (Rigaku, Tokyo, Japan) with Bragg-Brentano geometry (θ-2θ) and CuKα radiation (λ =0.154 nm) in the angle (2θ) range of 5^o to 40^o.

2.4. ATR-FTIR spectroscopy

ATR-FTIR spectra in the region of 750–4000 cm^{-1} were obtained using an IR-Prestige-21 FTIR spectrometer (Shimadzu, Japan) coupled with a Golden-Gate MKII ATR system (Specac, UK) equipped with a ZnSe lens after appropriate background subtraction. The resolution was two cm^{-1}, while sixty-four scans over the selected wavenumber range were averaged for each sample.

2.5. Multivariate analysis

2.5.1. Selection of spectral region and spectra data preprocessing

In ATR-FTIR measurements there are characteristic noisy regions (for example the region around 2360 cm^{-1}, corresponding to the atmospheric CO_2 absorption) that could result in significant source of variation and hence, poor correlation performance. For this reason, in the present study, the less noisy spectra regions, containing all the characteristic spectra peaks, were selected for performing the quantitative analysis (namely 800–1800 cm^{-1} and 2800–3500 cm^{-1}).

Data preprocessing on the mean spectrum (three replicate measurements were conducted) of each sample was performed in order to remove artifacts and undesirable information. Linear baseline correction and baseline offset were employed, in addition to mean centering, Savitzky-Golay smoothing (eleven smoothing points and third polynomial order filtering), standard normal variate (SNV) transformation and direct orthogonal signal correction (DOSC). The second derivative (which eliminates baseline drifts and enhances spectral differences) was also calculated via Savitzky -Golay filter with a window size of three points and a second order polynomial. All spectra preprocessing was performed using Matlab 2019b *v*. 9.7 (The Mathworks, Natick, MA, USA).

2.5.2. ANN regression

When developing machine learning models (such as ANNs), at a certain point, more features or dimensions can decrease model's accuracy (a phenomenon called 'the curse of dimensionality') (Han et al., 2020). In this case, a dimensionality reduction strategy (such as the utilization of PCA) may be employed in order to accelerate the training time of the model, reduce its complexity and avoid overfitting (Becker et al., 2020). In general, PCA projects the original data onto a new set of few variables called principal components (PCs). The first PC contains the greatest source of information, while each subsequent PC contains less information than the previous one (Ouiyangkul et al., 2020). PCA produces a matrix of the same dimensions of the original matrix, but the first few principal components contain a high percentage of the variance of the original data. Based on the above, in the present study the dimensionality reduction of the ANN's input space was performed through the utilization of PCA (i.e., instead of the whole spectrum a few major PCs were used as inputs). Each wavelength of ATR-FTIR spectra was treated as a variable during PCA and the singular value decomposition algorithm was employed to obtain the PCs, while a full model cross-validation was conducted via Matlab 2019b v. 9.7 (The Mathworks, Natick, MA). PCA score plots were used in order to evaluate whether the obtained data reduction (i.e. the use of PCs instead of the actual spectra) is able to differentiate among the two physical states of the API (i.e., amorphous and crystalline) and the ASDs (including the pure matrix carrier, SOL, itself).

In a further step, after dimensionality reduction, standard feed-forward (FF) back-propagation (BP) ANNs with multilayer perceptron architecture were tested. Initially, the data were divided into two subsets, a training set (consisting of twenty-two spectra) and a test set (containing of eight spectra), based on Kennard-Stone algorithm

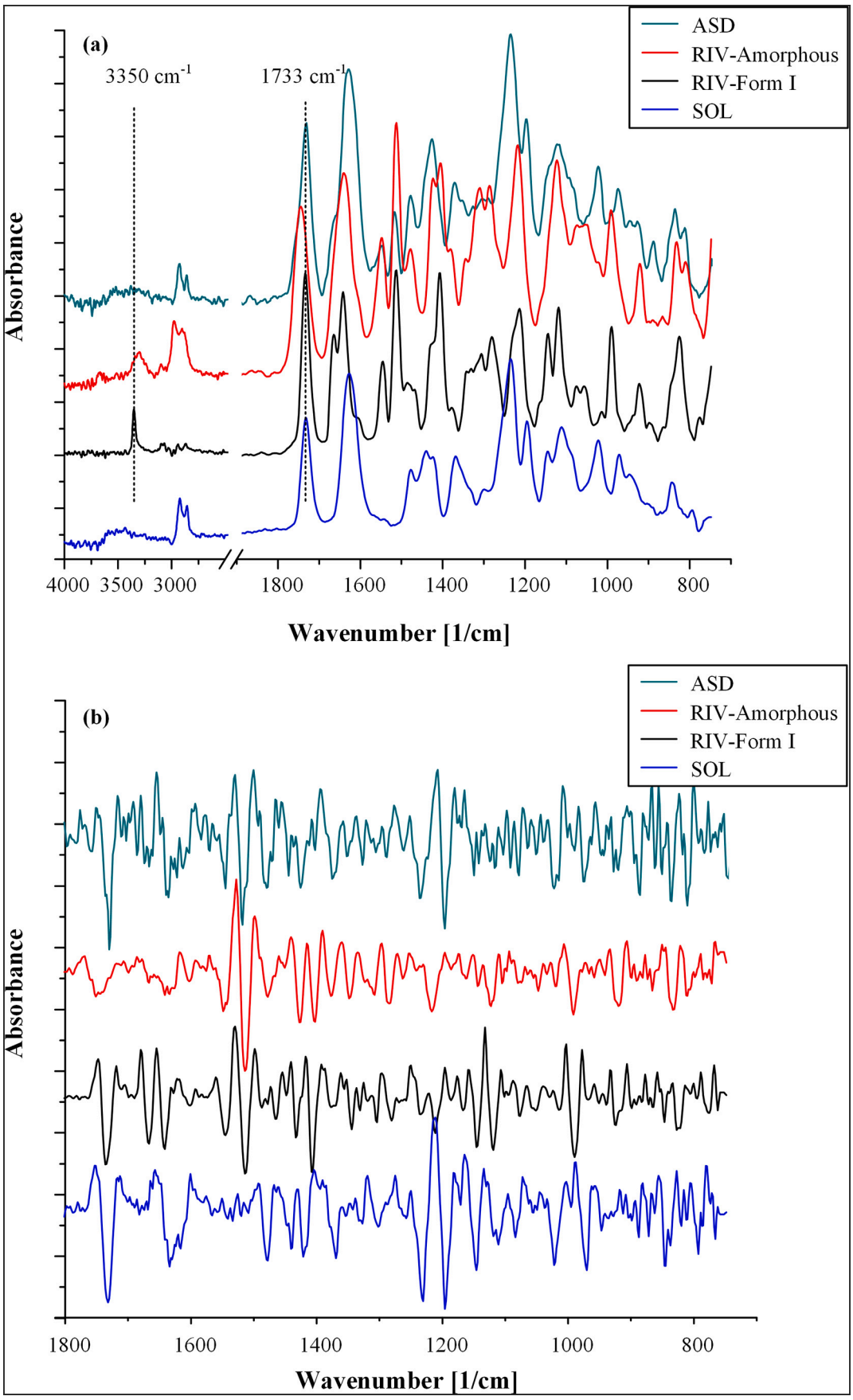

Fig. 1. ATR − FTIR spectra of pure crystalline RIV (form I), amorphous RIV, SOL and RIV − SOL ASDs as received (a) and after 2nd derivative transformation (b).

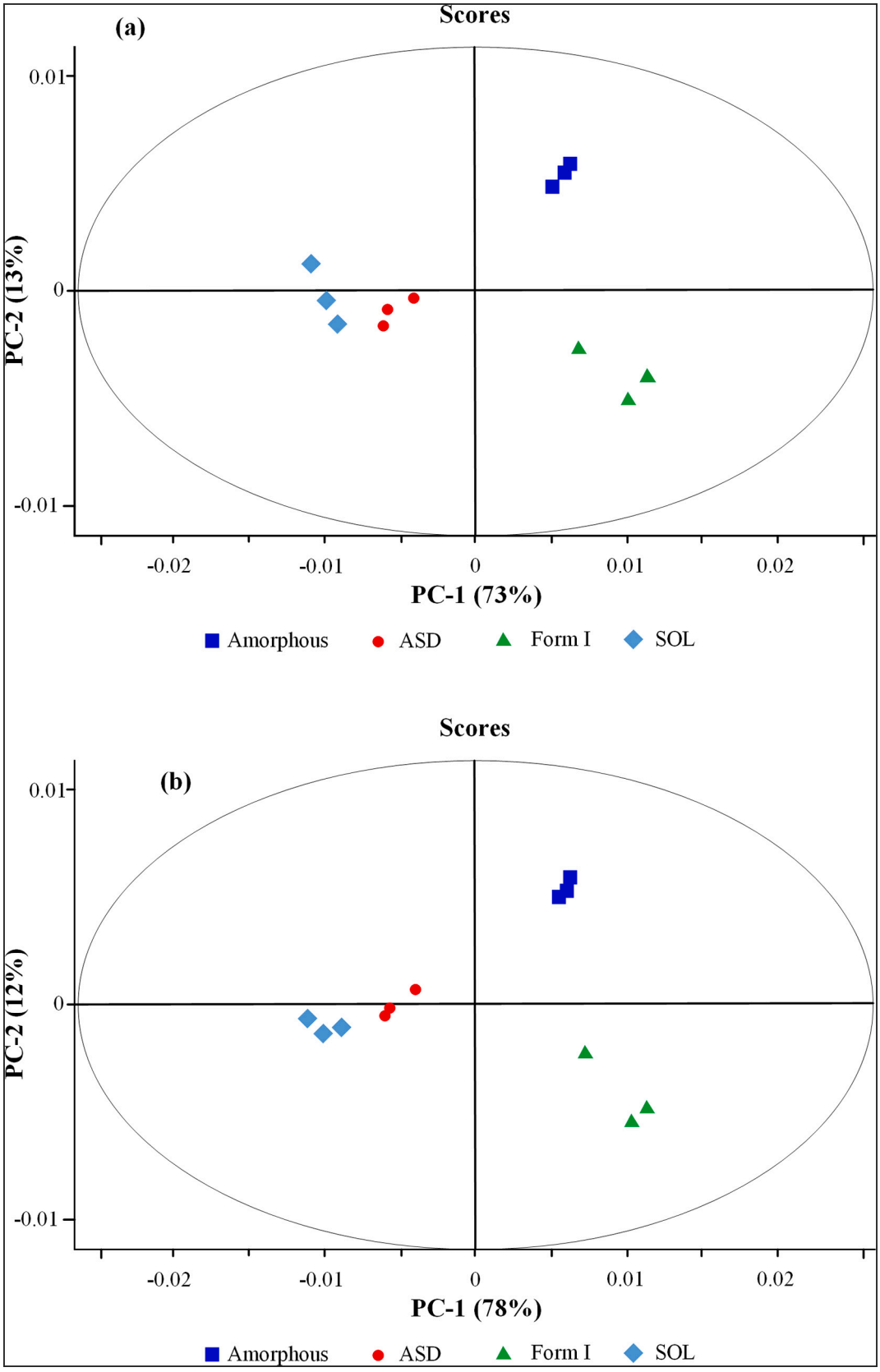

Fig. 2. Score plots of the PCA of the un-transformed (a) and the second derivative transformed (b) ATR-FTIR spectra of the ASDs, the matrix/carrier (SOL) and the amorphous and crystalline form I RIV.

(Kennard and Stone, 1969) (Table 1). Cross-validation by the leave-one-out method was applied in order to check the robustness of the method against the test set selection, while, in order to identify the factors that improve ANNs' prediction performance, design of experiments (DoE) methodology was employed. Specifically, a two-level full factorial design was selected with four (4) independent variables, namely: 1) the number of hidden units-neurons (X_1), 2) the level of iterating cycles (X_2), 3) the spectra region (X_3), and 4) the implementation of data transformation (i.e., 2nd derivative transformation or not, X_4). The root mean squared error of ANN's predictions (RMSEp) was used as a response (Oishi et al., 2020).

Table 2 shows the experimental domain along with the upper and lower levels examined for each factor. All experiments suggested by the employed DoE were conducted in a randomized order and in triplicate. Significant main factor and factors' interactions were estimated by employing analysis of variance (ANOVA) at a 0.05 significance level.

Based on the ANOVA results, linear regression models were constructed using multi-linear-regression (MLR):

$$Y_i = b_0 + b_1X_1 + b_2X_2 + b_3X_3 + b_4X_4 + b_{12}X_1X_2 + b_{13}X_1X_3 + b_{14}X_1X_4 + b_{23}X_2X_3 + b_{24}X_2X_4 + b_{34}X_3X_4 \quad (1)$$

where, Y_i is the response (i.e., ANN's RMSEp), b_0 is an intercept term, b_i to b_{ij} are regression coefficients for the main effects and two-way interactions, respectively, and $X_{1–4}$ are the coded levels of factors.

For all DoE experiments a single hidden layer using the scaled conjugate gradient (scg) method as training algorithm was used. Three ANN input variables were selected, namely the first three PCA components (PC1, PC2 and PC3). Training was repeated three times for each network and the average RMSEp and the corresponding standard deviation values were used. For the input to hidden layer and the hidden to output layer connections the logistic sigmoid transfer and the linear transfer functions were selected, respectively.

Netlab toolbox for Matlab was employed for the ANN modelling and training (Nabney, 2002), while DesignExpert® v.6.0.4 (Stat-Ease Inc., Minneapolis, MN) software package was used for the implementation of the DoE.

2.5.3. PCR and PLS regression

PCR and PLS regressions were selected as two standard widely applied regression methods for comparison with ANNs. The ChemoAC toolbox (Vandeginste and Smeyers-Verbeke, 2007) for Matlab was used and the optimum number of PCR and PLS components was automatically determined by a leave-one-out cross-validation procedure. RMSEp was used in order to evaluate the prediction performance of ANNs, while the validation and test sets were selected based on the Kennard-Stone algorithm.

3. Results and discussion

3.1. Verification of RIV's physical state

Before proceeding with the determination/quantification of the several physical states of RIV within the studied ASD system, the amorphization and the crystallinity of the drug was verified via pXRD. Fig. S1 (supplementary material) shows the diffractograms for the pure amorphous RIV, the prepared ASDs, as well as the mixture of the amorphous and the crystalline API with the prepared ASD systems. Results showed that the melting-quench cooling approach, followed for the preparation of the neat amorphous RIV and the ASDs, resulted in the full API amorphization since no pXRD peaks were recorded in the obtained diffractograms (only an amorphous halo was recorded). Additionally, the process followed for the mixing of the two API forms (i.e., the amorphous and crystalline RIV) did not alter their initial physical state, since no re-crystallization of the amorphous API or polymorphic transition for the crystalline API were observed.

3.2. ATR-FTIR characterization of neat starting materials and ASDs

Fig. 1 shows the ATR-FTIR spectra of the crystalline and the amorphous RIV, as well as the used matrix/carrier (SOL) and the ASDs. In respect to the crystalline API, results showed several characteristic peaks located at 3350 cm^{-1}, corresponding to secondary amide (N—H) stretching vibration; 1733 cm^{-1}, corresponding to C═O stretching from the ester group; 1670–1640 cm^{-1}, corresponding to the amide group stretching; 1575 - 1500 cm^{-1}, corresponding to Ar—Cl stretching and N—H scissoring; 1340–1000 cm^{-1}, corresponding to the C-O-C movement present in both ethers and esters, and 850–550 cm^{-1}, corresponding to C—Cl stretching, respectively. The obtained spectrum is in perfect agreement with a previously reported RIV form I spectrum (Xu et al., 2017). Compared to the crystalline RIV, the ATR-FTIR spectrum obtained for the neat amorphous API showed several significant differences. Concerning the amorphous API, the peak corresponding to the NH stretching of the amide group is significantly broaden and shifted in lower wavenumbers (from 3350 to 3313 cm^{-1}, respectively), while the peak corresponding to the -C=O stretching from the ester group of the API shows a shift from 1733 to 1745 cm^{-1}. In addition, there is a significant change at 1670–1640 cm^{-1} where one of the two characteristic peaks corresponding to the amide group stretching (the one at 1666 cm^{-1}) is now shown as a small shoulder shifted at 1658 cm^{-1}; while significant differences are also shown in the region of 1340–1000 cm^{-1}, which correspond to the C-O-C movement of the ether and the ester groups of the API. In regard to neat SOL, Fig. 1 shows strong absorption bands in the region of 1800 cm^{-1} and 1400 cm^{-1} reflecting the carbonyl stretching vibrations of the caprolactam ring. More precisely, the ATR-FTIR spectrum of SOL shows two characteristic peaks at 1635 and 1736 cm^{-1}, attributed to the -C=O stretching of the polyvinyl acetate group and the stretching of the -C(*O*)N or the tertiary amide of the polyvinyl caprolactam group, respectively. Finally, in the case of RIV-SOL ASDs the obtained spectrum showed that the peak corresponding to the secondary amide (-NH) stretching vibration of the API (located at 3350 and 3313 cm^{-1} for the crystalline and the amorphous API, respectively) is now completely missing, probably due to the formation of significant API-copolymer hydrogen bonds (HBs), while several differences are also observed in the rest spectrum compared to the neat SOL and the neat crystalline and amorphous API. Hence, the above described differences indicate that the obtained spectra are able to differentiate among the crystalline drug, its amorphous part and the ASD system. In addition, the utilization of 2nd derivative transformation also showed significant differences among the tested samples (Fig. 1b).

3.3. Quantification method results

Fig. 3 shows the ATR-FTIR spectra of the prepared ternary samples (Table 1) containing the crystalline and amorphous RIV along with the ASDs at different weight ratios. In all cases, spectra analysis showed that the increasing amount of crystalline and amorphous RIV concentrations leads to the increase of their specific ATR-FTIR peak intensities, although it is important to note that regarding the 2nd derivative transformations, these spectral differences are hard to be identified in the region of 2800–3500 cm^{-1}.

3.3.1. ANN regression

In order to accelerate ANN's training time, reduce its complexity and avoid overfitting, the input's space dimensionality (i.e., the ATR-FTIR data) was reduced through the implementation of PCA. However, before proceeding with the development of the ANN model, it is crucial to verify whether this data reduction strategy (i.e. the use of the major PCs instead of the actual collected spectra) is able to differentiate among the two physical states of the API (i.e., the amorphous and crystalline RIV) and the ASDs system (including the pure matrix carrier, SOL). In order to do so, PCA score plots were constructed for both the untransformed and the 2nd derivative transformed spectra (Fig. 2a and b

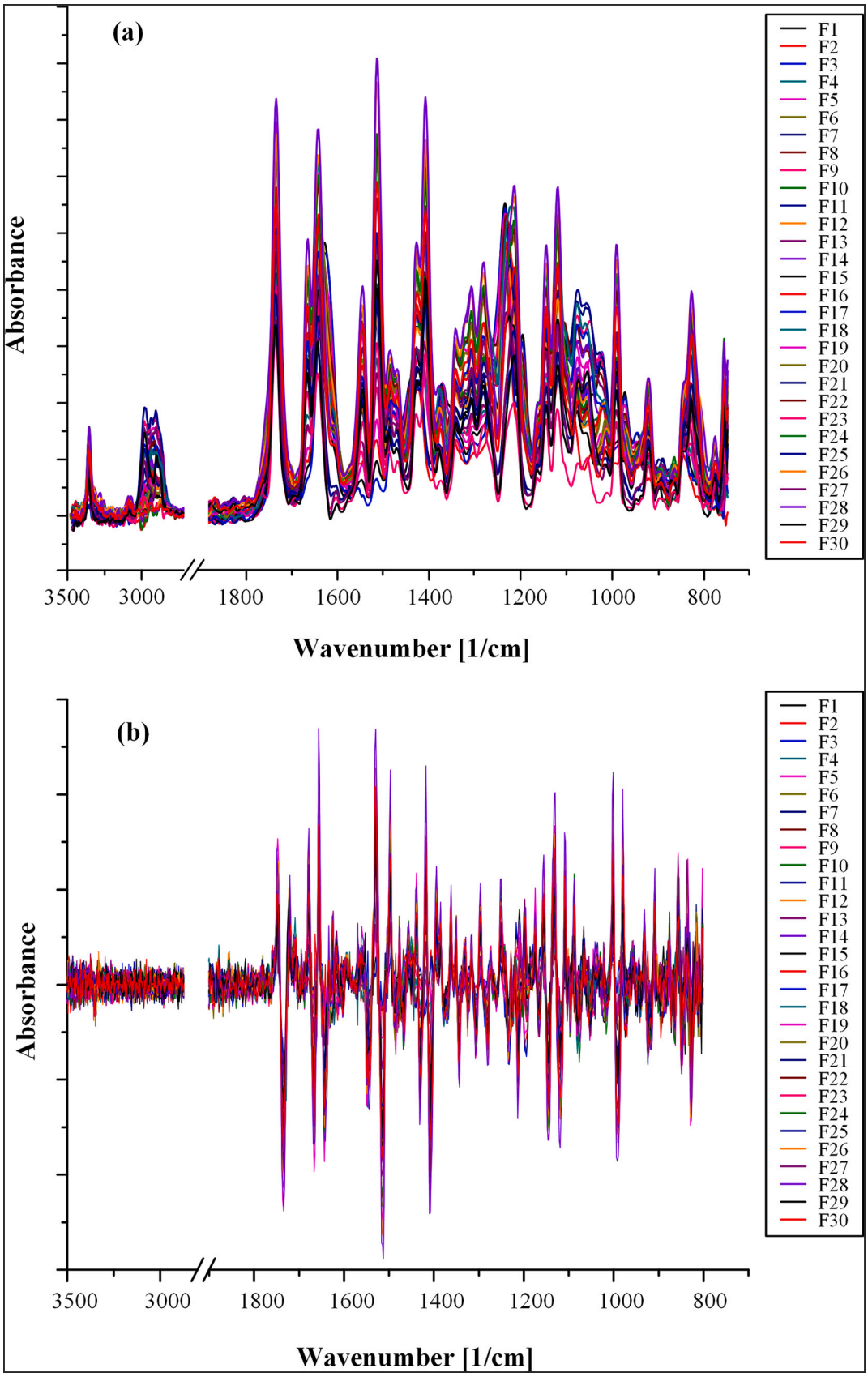

Fig. 3. Un-transformed (a) and 2nd derivate (b) ATR-FTIR spectra of samples containing the crystalline RIV, the amorphous RIV and the ASDs according to Table 1.

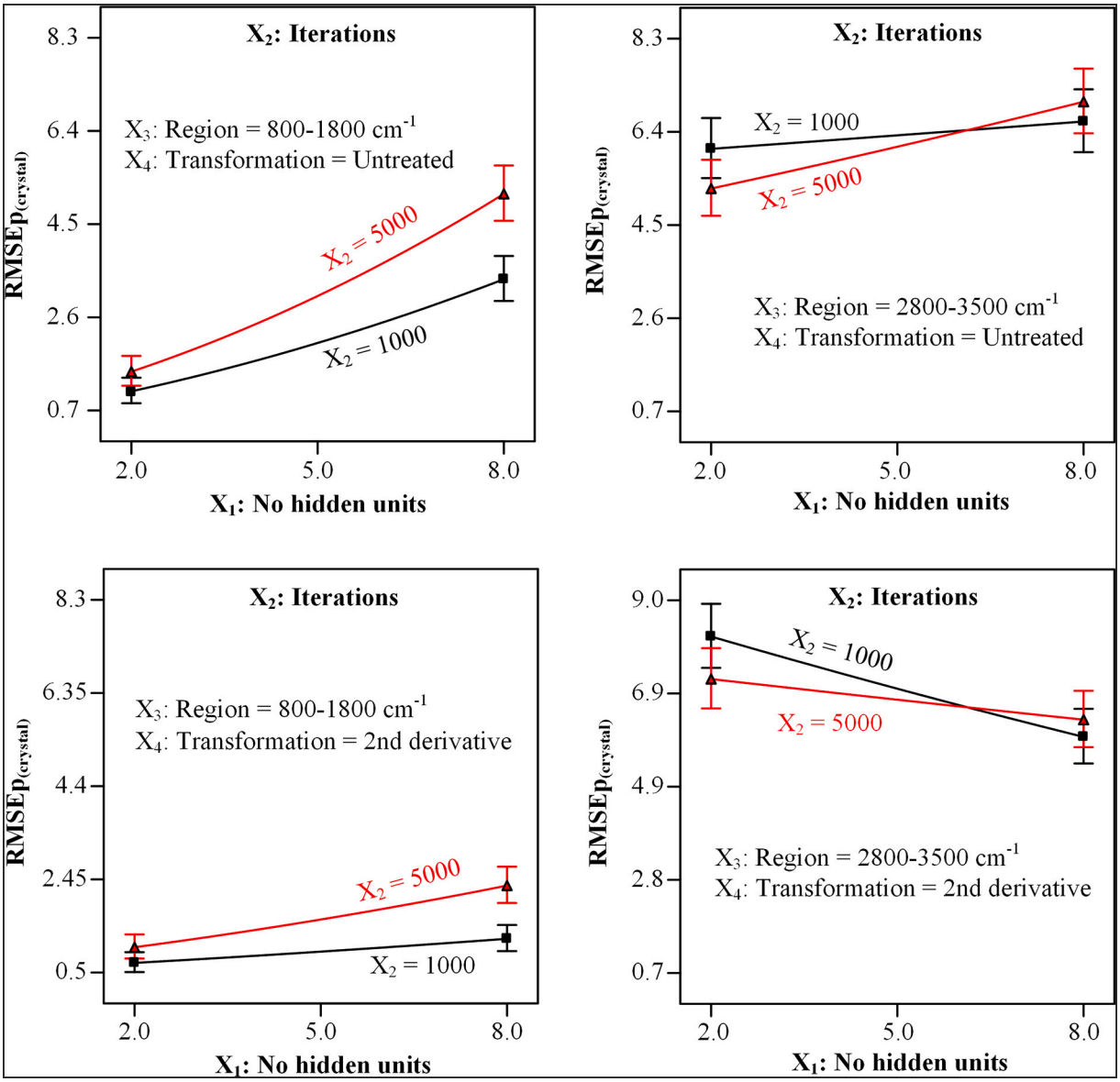

Fig. 4. Two-way interaction effect plots based on the full-factorial experimental design employed for the determination of crystalline RIV within the ASD system.

respectively). Results showed that in both cases separate individual clusters were recorded, indicating that PCA data reduction is able to differentiate among the several components. Additionally, results indicate that the use of the first component (PC1) is able to separate the API (either crystalline or amorphous) from the copolymer (SOL) and the ASD system, while the use of the second component (PC2) is able to differentiate between the two different API physical states. Hence, based on these obtained results, the utilization of PCA as an ANN dimensionality reduction strategy does not compromise the ability of the data to differentiate among the several API physical states and the ASD. Furthermore, in both cases (i.e., un-transformed and 2nd derivative transformed data) PCA showed that the three first PCs were able to explain almost the 97% variation of the data, meaning that these three components (i.e., PC1, PC2 and PC3) are adequate enough for ANN's dimensionality reduction.

In a further step, after ANN's input dimensionality reduction, a two-level full factorial DoE was employed in order to determine ANN's optimum number of hidden units and level of iteration cycles, as well as the optimum spectra region which leads to enhanced ANN predictions performance. Additionally, through the use of the selected DoE, the effect of 2nd derivative spectra transformation on the generalizing ability of the ANN model was also evaluated. Table 2 shows the ANN-derived RMSEp values for the crystalline and amorphous quantification of the test set based on the employed two-level full-factorial DoE, while the RSME of prediction for the training set was below 0.05. Concerning the crystalline API, results varied from 0.86 (using 5 hidden nodes, 3000 iteration cycles, 800–1800 cm^{-1} spectral region and 2nd derivative transformation) to 7.50 (using 2 hidden nodes, 5000 iteration cycles, 2800–3500 cm^{-1} spectral region and 2nd derivative transformation), while for amorphous RIV results varied from 2.14 (using 2 hidden nodes, 1000 iteration cycles, 800–1800 cm^{-1} spectral region and no data transformation) to 12.91 (using 5 hidden nodes, 3000 iteration cycles, 800–1800 cm^{-1} spectral region and no data transformation). These results indicate that the selection of the appropriate spectra region, ANN training/structure parameters and data transformation, is able to significantly improve ANN's goodness of fit during the quantification of both the crystalline and the amorphous API parts present within the ASD system.

ANOVA results for the employed full-factorial experimental design are summarized in Table 3. A significance level of 0.05 was used for all main and interaction effects, while the square root transformation (i.e., $Y = (RMSEp)^{1/2}$) and the inverse square root transformation (i.e., $Y = 1/$

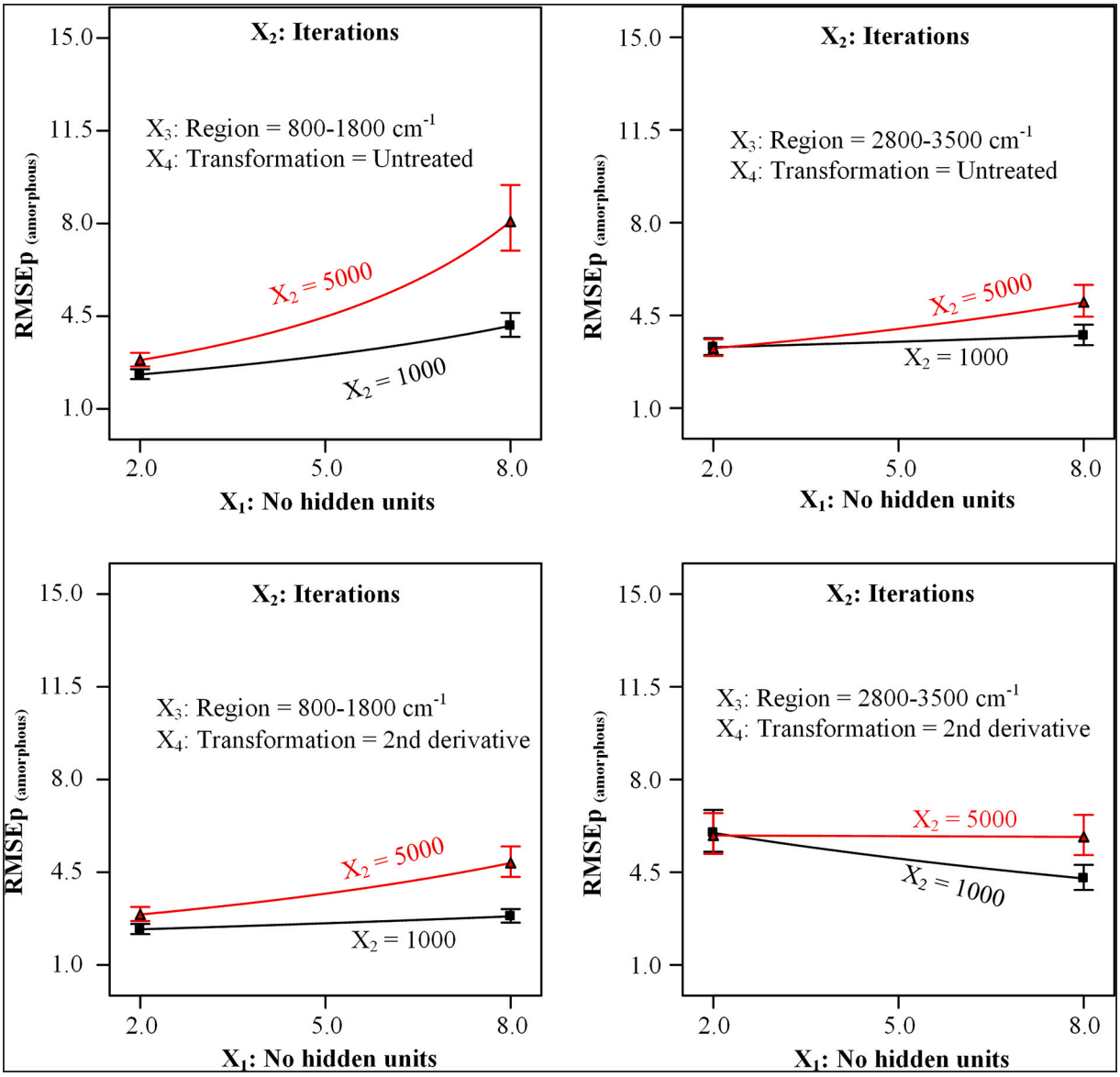

Fig. 5. Two-way interaction effect plots based on the full-factorial experimental design employed for the determination of amorphous RIV within the ASD system.

$(RMSEp)^{1/2}$) were used for the crystalline and the amorphous API results, respectively, based on Box-Cox plot analysis in order to meet the assumptions that make the ANOVA analysis valid (interval data of the dependent variable, normality, homoscedasticity, and no multi-co-linearity). The adequate precision (depicts the value of signal to noise ratio; ratio greater than 4 is preferred), the coefficient of variation (CV) (measures the reproducibility of the model; a value less than 10% is desirable), and the *p*-value of the models ($p < 0.05$ is needed) were all in the desirable limits. ANOVA results indicated that, regarding crystalline API, all factors examined had a significant effect on ANN's prediction performance, while in the case of amorphous RIV, data transformation (X_4) was not crucial, although it was involved in several statistically significant interactions. In both cases (i.e., determination of crystalline and amorphous API within the ASD system), several two-way interactions, such as X_1X_2, X_1X_3, X_1X_4, X_2X_3 and X_3X_4, were identified as having a statistically significant impact on the measured responses. Based on the ANOVA results, the following two MLR models were constructed, after the removal of insignificant terms by a backward elimination process (alpha out = 0.05):

$$\left[RMSEp_{(crystal)}\right]^{1/2} = -1.96 + 0.15 \times_1 + 0.064 \times_2 + 0.60 \times_3 - 0.084 \times_4 + 0.062X_1X_2 - .0.17X_1X_3 - 0.13X_1X_4 - 0.087X_2X_3 + 0.15X_3X_4 \quad (2)$$

$$1 \Big/ \left[RMSEp_{(amorphous)}\right]^{1/2} = 0.51 - 0.041 \times_1 - 0.034 \times_2 - 0.037 \times_3 - 9.9E-003 \times_4 - . 0.018X_1X_2 + 0.034X_1X_3 + 0.027X_1X_4 + 0.017X_2X_3 - 0.034X_3X_4 \quad (3)$$

In the above fitting equations, all factors are given in coded forms (−1 to 1), while the second model (i.e., the fitting equation corresponding to the amorphous API) was hierarchically corrected in order to include the insignificant main 'parental' factor X_4. Correlation coefficient (R^2) values for the fitting equations corresponding to the crystalline and the amorphous API were 0.94 and 0.85, respectively, indicating a better fitting in the case of the crystalline API.

Fig. 4 shows the two-way interaction plots for the MLR fitting equation corresponding to the crystalline RIV content within the ASD system. Results showed that in the spectral region of 800–1800 cm^{-1} the

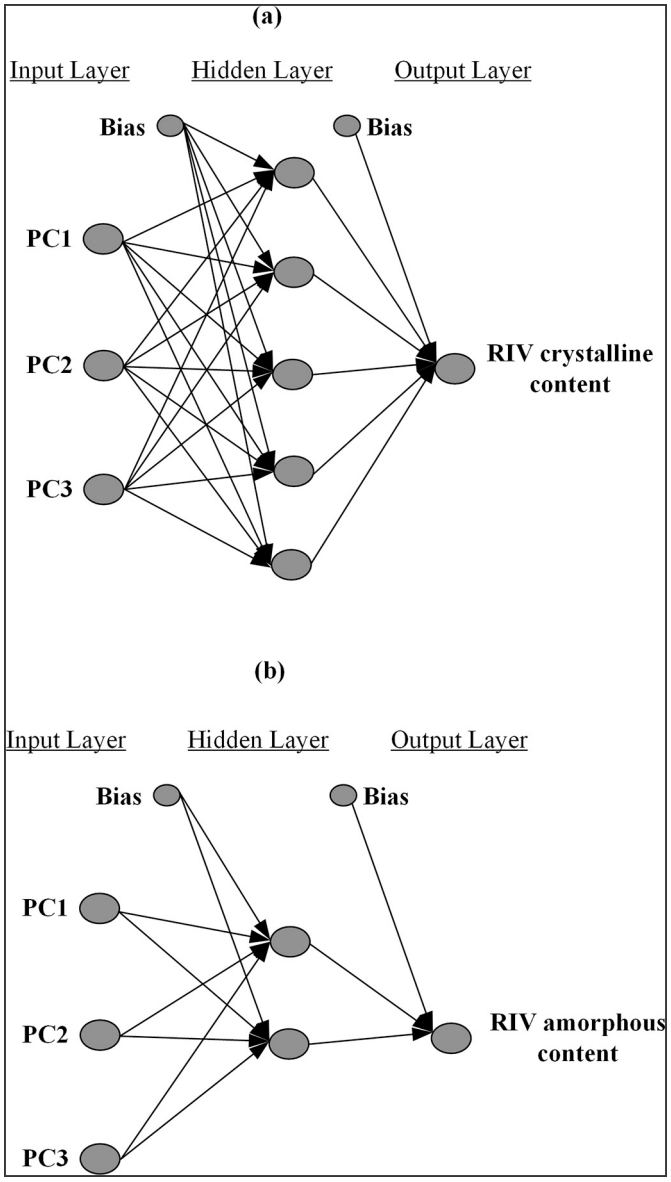

Fig. 6. Optimal ANN architecture for the determination of the crystalline (a) and the amorphous (b) RIV content within the prepared RIV-SOL ASDs.

Table 3
ANOVA results for the employed full factorial design (0.05 significance probability level).

Factors	Crystalline		Amorphous	
	F-value	p-value	F-value	p-value
X_1	28.30	< 0.0001[a]	46.34	< 0.0001[a]
X_2	4.77	0.0342[a]	31.36	< 0.0001[a]
X_3	429.41	< 0.0001[a]	37.39	< 0.0001[a]
X_4	8.40	0.0058[a]	2.66	0.1097[b]
X_1X_2	4.53	0.0388[a]	9.11	0.0042[a]
X_1X_3	34.34	< 0.0001[a]	30.49	< 0.0001[a]
X_1X_4	20.91	< 0.0001[a]	19.87	< 0.0001[a]
X_2X_3	8.91	0.0046[a]	8.16	0.0064[a]
X_2X_4	0.26	0.6119	2.43	0.1260
X_3X_4	27.40	< 0.0001[a]	30.91	< 0.0001[a]

[a] significant factors
[b] parental factors included into the MLR models

Table 4
RMSEp for PCR and PLS regression fitting.

	RMSEp			
	No-transformation		2nd derivative	
	800–1800 cm^{-1}	2800–3500 cm^{-1}	800–1800 cm^{-1}	2800–3500 cm^{-1}
PCR				
Crystalline	9.60	7.42	9.94	11.41
Amorphous	10.12	15.83	13.45	17.96
PLS				
Crystalline	9.48	9.50	11.89	14.30
Amorphous	17.86	15.15	13.15	16.50

increasing number of ANN's hidden units results in a diminishing of network's prediction ability (i.e., increase in $RMSEp_{(crystal)}$), irrespectively of the iteration cycles used or the selection of spectral data transformation. Additionally, results depicted that decreasing iteration cycles (from 5000 to 1000) causes in a reduction of $RMSEp_{(crystal)}$, indicating that the increasing iterations may lead to network's overfitting. In contrast to these findings, when the 2800–3500 cm^{-1} spectral region was evaluated for the development of the ANN model, increasing iteration cycles lead to an improvement of network's prediction ability at low number of hidden units (i.e., below five). In addition, increasing number of hidden units resulted in a reduction of $RMSEp_{(crystal)}$ values only in the case of 2nd derivative transformations.

Regarding amorphous API, results from the two-way interaction plots presented in Fig. 5 showed that in the spectral region of 800–1800 cm^{-1}, the increasing number of ANN's hidden units provoke a reduction of ANN's prediction performance, irrespectively of data transformation, only for high number of iteration cycles (i.e., 5000). Concerning, low iterations (i.e., 1000), increasing network's hidden units had a limited effect in network's performance (mostly when untreated spectral data were used). Similar results were observed for 2800–3500 cm^{-1} spectral region with no data transformation, while when 2nd derivative transformation was applied, network's performance was improved only in the case of low iteration cycles.

Based on the above analysis, the best fitting performance concerning the crystalline RIV was achieved using five hidden units, at 3000 iteration cycles, when the 800–1800 cm^{-1} spectral region was used and the spectra data were transformed using the 2nd derivative transformations. Similarly, regarding the amorphous API the best results were obtained when the fitting was performed using the 800–1800 cm^{-1} spectral region, with no data transformation and the network consists of two hidden units trained at 1000 iterations. Both models are graphically depicted in Fig. 6.

3.3.2. PCR and PLS regression

In addition to neural networks, PCR and PLS regression models were also constructed and their fitting performance was evaluated for comparison reasons. Similarly, to the ANNs case, data transformation using the 2nd derivative, as well as the use of two separate spectra regions (i.e., 800–1800 and 2800–3500 cm^{-1}) were also evaluated. Since the quality of the fitting models depends highly upon the number of the latent variables (LV) chosen (i.e., too few factors may lead to underfitting, while too many factors may lead to overfitting) for the construction of the PCR and PLS regression models, the optimum number of LVs was carefully selected based on the lowest RMSE value for cross-validation and the predicted residual error sum of squares.

Table 4 shows the prediction performance (measured in terms of RMSEp) for the two regression models. In the case of PCR, the lowest RMSEp value for the determination of the crystalline API was obtained when the 2800–3500 cm^{-1} part of the FTIR spectrum was evaluated with no data transformation ($RMSEp_{(crystal)} = 7.42$). This is in agreement with the analysis of the obtained spectra, where the most significant difference between the crystalline API and the ASD system, or the neat

amorphous API, was observed in the NH stretching of the amide group, located at 3350 cm^{-1}. In contrast, for the determination of the neat amorphous API, the lowest RMSEp value (i.e., 10.12) was observed when the 800–1800 cm^{-1} part of the FTIR spectrum was used (again with no data-transformation), which is in agreement with the previous ATR-FTIR analysis, showing that the neat amorphous API and the ASDs present only limited differences in the 2800–3500 cm^{-1} part of the FTIR spectrum. Similarly, PLS regression fitting for the crystalline API showed the best prediction performance when the 800–1800 cm^{-1} part of the FTIR spectrum was used with no-data transformation ($RMSEp_{(crystal)}$ = 7.89), while the respective best fitting for the amorphous API was obtained when 2nd derivative transformations were employed. Finally, the comparison of the obtained results for the two different models, showed improved prediction performance in the case of PCR, compared to PLS regression, with lower RMSEp values obtained for both the crystalline and the amorphous API.

3.3.3. Comparison of ANNs and PLS fitting

The comparison of the fitting results for all developed models revealed a significant superiority for ANN-based regression. Specifically, for the determination of the crystalline API, the $RMSEp_{(crystal)}$ for the ANN fitting model was 0.86, compared to 7.42 and 9.48 obtained from the PCR and PLS, respectively; while concerning the neat amorphous API, ANNs showed a $RMSEp_{(amorphous)}$ value of 2.69, which is significantly lower compared to the 10.12 and 13.15 values obtained from PCR and PLS regression models, respectively. This remarkable superiority of ANN's prediction performance can be attributed to its inherent non-linear generalizing ability, as well as, its ability to be trained directly from the data used (Barmpalexis et al., 2018). Especially in cases where the simultaneous determination of the crystalline and the amorphous API is evaluated (such as in the present study) and hence, there is increased peak/signal overlapping due to enhanced structural similarity between the investigated compounds (i.e., the crystalline and the amorphous forms of the same compound), the need of more powerful/sophisticated regression techniques, such as ANNs, seems to significantly surpass the performance of traditionally used regression tools, such as PCR and PLS regression.

4. Conclusion

In this study, ANNs combined with ATR-FTIR spectroscopy were able to provide a new chemometric tool for simultaneous determination and quantification of the percentage of the crystalline and the amorphous API located within the drug-rich amorphous zones in ASDs. Implementation of a DoE screening revealed that the proper setting of several ANN parameters (i.e., number of hidden units and iteration cycles), along with the appropriate selection of the IR spectral region and data preprocessing may significantly improve model's prediction performance. Finally, comparison with traditionally used regression techniques, such as PCR and PLS regression, revealed the increased superiority of ANNs, which can be attributed to their inherent ability to handle efficiently non-linear relationships, a feature extremely important in samples where increased peak/signal overlapping is observed. This new ANN-based model can be potentially used to evaluate ASD's physical stability profile during storage, or to achieve an improved on-line control over manufacturing processes in the framework of the process analytical technology.

Declaration of Competing Interest

The authors report no declarations of interest

Acknowledgments

None.

Appendix A. Supplementary data

Supplementary data to this article can be found online at https://doi.org/10.1016/j.ijpx.2020.100064.

References

Arabzadeh, V., Sohrabi, M.R., Goudarzi, N., Davallo, M., 2019. Using artificial neural network and multivariate calibration methods for simultaneous spectrophotometric analysis of Emtricitabine and Tenofovir alafenamide fumarate in pharmaceutical formulation of HIV drug. Spectrochim. Acta A Mol. Biomol. Spectrosc. 215, 266–275.
Barmpalexis, P., Karagianni, A., Nikolakakis, I., Kachrimanis, K., 2018. Artificial neural networks (ANNs) and partial least squares (PLS) regression in the quantitative analysis of cocrystal formulations by Raman and ATR-FTIR spectroscopy. J. Pharm. Biomed. Anal. 158, 214–224.
Baskin, I.I., Winkler, D., Tetko, I.V., 2016. A renaissance of neural networks in drug discovery. Expert Opin. Drug Discovery 11, 785–795.
Becker, M., Lippel, J., Stuhlsatz, A., Zielke, T., 2020. Robust dimensionality reduction for data visualization with deep neural networks. Graph. Model. 108, 101060.
Bugay, D.E., 2001. Characterization of the solid-state: spectroscopic techniques. Adv. Drug Deliv. Rev. 48, 43–65.
Costa, L.R., Tonoli, G.H.D., Milagres, F.R., Hein, P.R.G., 2019. Artificial neural network and partial least square regressions for rapid estimation of cellulose pulp dryness based on near infrared spectroscopic data. Carbohydr. Polym. 224, 115186.
Dedroog, S., Huygens, C., Van den Mooter, G., 2019. Chemically identical but physically different: a comparison of spray drying, hot melt extrusion and cryo-milling for the formulation of high drug loaded amorphous solid dispersions of naproxen. Eur. J. Pharm. Biopharm. 135, 1–12.
Edinger, M., Knopp, M.M., Kerdoncuff, H., Rantanen, J., Rades, T., Löbmann, K., 2018. Quantification of microwave-induced amorphization of celecoxib in PVP tablets using transmission Raman spectroscopy. Eur. J. Pharm. Sci. 117, 62–67.
Guo, Y., Shalaev, E., Smith, S., 2013. Physical stability of pharmaceutical formulations: solid-state characterization of amorphous dispersions. TrAC Trends Anal. Chem. 49, 137–144.
Han, J., Lu, J., Zhou, M., 2020. Solving high-dimensional eigenvalue problems using deep neural networks: a diffusion Monte Carlo like approach. J. Comput. Phys. 423, 109792.
Huang, S., Williams 3rd, R.O., 2018. Effects of the preparation process on the properties of amorphous solid dispersions. AAPS PharmSciTech 19, 1971–1984.
Kawakami, K., 2017. Supersaturation and crystallization: non-equilibrium dynamics of amorphous solid dispersions for oral drug delivery. Expert Opinion Drug Deliv. 14, 735–743.
Kennard, R.W., Stone, L.A., 1969. Computer aided design of experiments. Technometrics 11, 137–148.
Lin, X., Hu, Y., Liu, L., Su, L., Li, N., Yu, J., Tang, B., Yang, Z., 2018. Physical stability of amorphous solid dispersions: a physicochemical perspective with thermodynamic, kinetic and environmental aspects. Pharm. Res. 35, 125.
Lust, A., Strachan, C.J., Veski, P., Aaltonen, J., Heinämäki, J., Yliruusi, J., Kogermann, K., 2015. Amorphous solid dispersions of piroxicam and Soluplus®: Qualitative and quantitative analysis of piroxicam recrystallization during storage. Int. J. Pharm. 486, 306–314.
Meng, F., Meckel, J., Zhang, F., 2017. Investigation of itraconazole ternary amorphous solid dispersions based on povidone and Carbopol. Eur. J. Pharm. Sci. 106, 413–421.
Nabney, I., 2002. NETLAB: Algorithms for Pattern Recognition. Springer.
Nagy, B., Petra, D., Galata, D.L., Démuth, B., Borbás, E., Marosi, G., Nagy, Z.K., Farkas, A., 2019. Application of artificial neural networks for Process Analytical Technology-based dissolution testing. Int. J. Pharm. 567, 118464.
Netchacovitch, L., Dumont, E., Cailletaud, J., Thiry, J., De Bleye, C., Sacré, P.Y., Boiret, M., Evrard, B., Hubert, P., Ziemons, E., 2017. Development of an analytical method for crystalline content determination in amorphous solid dispersions produced by hot-melt extrusion using transmission Raman spectroscopy: a feasibility study. Int. J. Pharm. 530, 249–255.
Newman, A., Nagapudi, K., Wenslow, R., 2015. Amorphous solid dispersions: a robust platform to address bioavailability challenges. Ther. Deliv. 6, 247–261.
Oishi, T., Hayashi, Y., Noguchi, M., Yano, F., Kumada, S., Takayama, K., Okada, K., Onuki, Y., 2020. Creation of novel large dataset comprising several granulation methods and the prediction of tablet properties from critical material attributes and critical process parameters using regularized linear regression models including interaction terms. Int. J. Pharm. 577, 119083.
Ouiyangkul, P., Tantishaiyakul, V., Hirun, N., 2020. Exploring potential coformers for oxyresveratrol using principal component analysis. Int. J. Pharm. 587, 119630.
Pandi, P., Bulusu, R., Kommineni, N., Khan, W., Singh, M., 2020. Amorphous solid dispersions: an update for preparation, characterization, mechanism on bioavailability, stability, regulatory considerations and marketed products. Int. J. Pharm. 586, 119560.
Paudel, A., Geppi, M., Mooter, G.V.D., 2014. Structural and dynamic properties of amorphous solid dispersions: the role of solid-state nuclear magnetic resonance spectroscopy and relaxometry. J. Pharm. Sci. 103, 2635–2662.
Perzborn, E., Roehrig, S., Straub, A., Kubitza, D., Mueck, W., Laux, V., 2010. Rivaroxaban: a new oral factor Xa inhibitor. Arterioscler. Thromb. Vasc. Biol. 30, 376–381.
Purohit, H.S., Taylor, L.S., 2015. Phase separation kinetics in amorphous solid dispersions upon exposure to water. Mol. Pharm. 12, 1623–1635.

Rahman, Z., Zidan, A.S., Khan, M.A., 2010. Formulation and evaluation of a protein-loaded solid dispersions by non-destructive methods. AAPS J. 12, 158–170.
Rahman, Z., Siddiqui, A., Bykadi, S., Khan, M.A., 2014. Near-infrared and fourier transform infrared chemometric methods for the quantification of crystalline tacrolimus from sustained-release amorphous solid dispersion. J. Pharm. Sci. 103, 2376–2385.
Ricarte, R.G., Van Zee, N.J., Li, Z., Johnson, L.M., Lodge, T.P., Hillmyer, M.A., 2019. Recent advances in understanding the micro- and nanoscale phenomena of amorphous solid dispersions. Mol. Pharm. 16, 4089–4103.
Rumondor, A.C.F., Taylor, L.S., 2010. Application of Partial Least-Squares (PLS) modeling in quantifying drug crystallinity in amorphous solid dispersions. Int. J. Pharm. 398, 155–160.
Saerens, L., Dierickx, L., Lenain, B., Vervaet, C., Remon, J.P., Beer, T.D., 2011. Raman spectroscopy for the in-line polymer–drug quantification and solid state characterization during a pharmaceutical hot-melt extrusion process. Eur. J. Pharm. Biopharm. 77, 158–163.
Samama, M.M., 2011. The mechanism of action of rivaroxaban–an oral, direct factor Xa inhibitor–compared with other anticoagulants. Thromb. Res. 127, 497–504.
Sarpal, K., Delaney, S., Zhang, G.G.Z., Munson, E.J., 2019. Phase behavior of amorphous solid dispersions of felodipine: homogeneity and drug-polymer interactions. Mol. Pharm. 16, 4836–4851.
Sibik, J., Löbmann, K., Rades, T., Zeitler, J.A., 2015. Predicting crystallization of amorphous drugs with terahertz spectroscopy. Mol. Pharm. 12, 3062–3068.
Siddiqui, A., Rahman, Z., Bykadi, S., Khan, M.A., 2014. Chemometric methods for the quantification of crystalline tacrolimus in solid dispersion by powder X-ray diffractometry. J. Pharm. Sci. 103, 2819–2828.
Song, Y., Zemlyanov, D., Chen, X., Nie, H., Su, Z., Fang, K., Yang, X., Smith, D., Byrn, S., Lubach, J.W., 2016. Acid-Base interactions of polystyrene sulfonic acid in amorphous solid dispersions using a combined UV/FTIR/XPS/ssNMR Study. Mol. Pharm. 13, 483–492.
Toziou, P.M., Barmpalexis, P., Boukouvala, P., Verghese, S., Nikolakakis, I., 2018. Quantification of live Lactobacillus acidophilus in mixed populations of live and killed by application of attenuated reflection Fourier transform infrared spectroscopy combined with chemometrics. J. Pharm. Biomed. Anal. 154, 16–22.
Vandeginste, B., Smeyers-Verbeke, J., 2007. ChemoAC: its contribution to the advancement of chemometrics. J. Chemom. 21, 257–262.
Wabuyele, B.W., Sotthivirat, S., Zhou, G.X., Ash, J., Dhareshwar, S.S., 2017. Dispersive raman spectroscopy for quantifying amorphous drug content in intact tablets. J. Pharm. Sci. 106, 579–588.
Wlodarski, K., Zhang, F., Liu, T., Sawicki, W., Kipping, T., 2018. Synergistic effect of polyvinyl alcohol and copovidone in itraconazole amorphous solid dispersions. Pharm. Res. 35, 16.
Xu, Y., Wu, S.-P., Liu, X.-J., Zhang, L.-J., Lu, J., 2017. Crystal characterization and transformation of the forms I and II of anticoagulant drug rivaroxaban. Cryst. Res. Technol. 52, 1600379.
Xu, Y., Yao, H., Lin, K., 2018. An overview of neural networks for drug discovery and the inputs used. Expert Opin. Drug Discovery 13, 1091–1102.
Yang, X., Wang, Y., Byrne, R., Schneider, G., Yang, S., 2019. Concepts of artificial intelligence for computer-assisted drug discovery. Chem. Rev. 119, 10520–10594.
Zidan, A.S., Rahman, Z., Sayeed, V., Raw, A., Yu, L., Khan, M.A., 2012. Crystallinity evaluation of tacrolimus solid dispersions by chemometric analysis. Int. J. Pharm. 423, 341–350.